MICROROBOTS

Elucidating the interaction dynamics between microswimmer body and immune system for medical microrobots

Immihan Ceren Yasa[1]*, Hakan Ceylan[1]*, Ugur Bozuyuk[1], Anna-Maria Wild[1], Metin Sitti[1,2]†

The structural design parameters of a medical microrobot, such as the morphology and surface chemistry, should aim to minimize any physical interactions with the cells of the immune system. However, the same surface-borne design parameters are also critical for the locomotion performance of the microrobots. Understanding the interplay of such parameters targeting high locomotion performance and low immunogenicity at the same time is of paramount importance yet has so far been overlooked. Here, we investigated the interactions of magnetically steerable double-helical microswimmers with mouse macrophage cell lines and splenocytes, freshly harvested from mouse spleens, by systematically changing their helical morphology. We found that the macrophages and splenocytes can recognize and differentially elicit an immune response to helix turn numbers of the microswimmers that otherwise have the same size, bulk physical properties, and surface chemistries. Our findings suggest that the structural optimization of medical microrobots for the locomotion performance and interactions with the immune cells should be considered simultaneously because they are highly entangled and can demand a substantial design compromise from one another. Furthermore, we show that morphology-dependent interactions between macrophages and microswimmers can further present engineering opportunities for biohybrid microrobot designs. We demonstrate immunobots that can combine the steerable mobility of synthetic microswimmers and the immunoregulatory capability of macrophages for potential targeted immunotherapeutic applications.

INTRODUCTION

Untethered medical mobile robots on the size scale of a single cell can leverage minimally invasive targeted therapies at hard-to-reach, tight, and delicate body sites, such as the central nervous system, vascular system, and fetus (*1*–*3*). To realize such potential, a number of fully synthetic and biohybrid microrobot design approaches have been proposed in various forms that have combined locomotion, sensing, and response capabilities for specific requirements of a given target medical application (*4*–*6*). However, in vivo physiological environments present a variety of physical, chemical, and biological barriers to protect the body from external detriments, which could impair the efficient and safe intervention of untethered medical microrobots (*7*). When a microrobot is deployed inside the human body, similar to any other foreign material, it is often regarded as an intruder, and an immune response is elicited to eliminate it. This protection mechanism is mediated by nonspecific (innate) and specific (adaptive) responses that are composed of different cell types, which take part in a predetermined order and in close communication and coordination between cells (*8*). In the first line, the cells of the innate immune system, including macrophages, recognize and neutralize the intruders by physically engaging them with a process called phagocytosis and elucidating a generic communication response in the form of various cytokines.

Macrophages are central to the immune system. They reside stationary in the tissues, e.g., splenic red pulp, microglia, and Kupffer cells in the liver or their precursor form (monocytes) are mobile in the bloodstream to infiltrate the pathology sites, e.g., a new-forming tumor (*9*). The interaction of macrophages with nanoparticles has been under heavy investigation because they are responsible for the rapid clearance of therapeutic nanoparticles from the blood circulation (*10*). The efficiency of this process was reported to be based on the surface chemistry, size, shape, and orientation of the interaction with the intruder (*10*, *11*). If the measures taken by this defense do not suffice, then macrophages can also use the chemical information obtained from the engulfed intruders to train T lymphocytes and to release cytokines for the development and differentiation of T and B lymphocytes. T and B lymphocytes can engage the

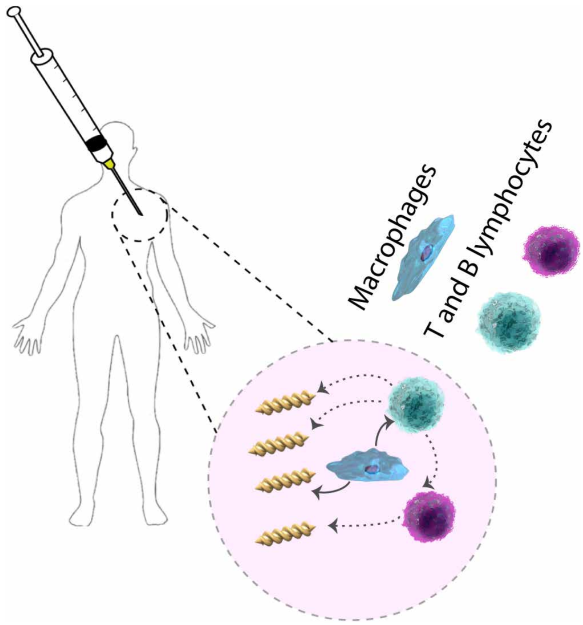

Movie 1. Summary of microswimmer–immune system interactions.

---

[1]Physical Intelligence Department, Max Planck Institute for Intelligent Systems, 70569 Stuttgart, Germany. [2]School of Medicine and School of Engineering, Koç University, 34450 Istanbul, Turkey.
*These authors contributed equally to this work as co-first authors.
†Corresponding author. Email: sitti@is.mpg.de

intruder at the second line using more effective and specific weaponry (*8*).

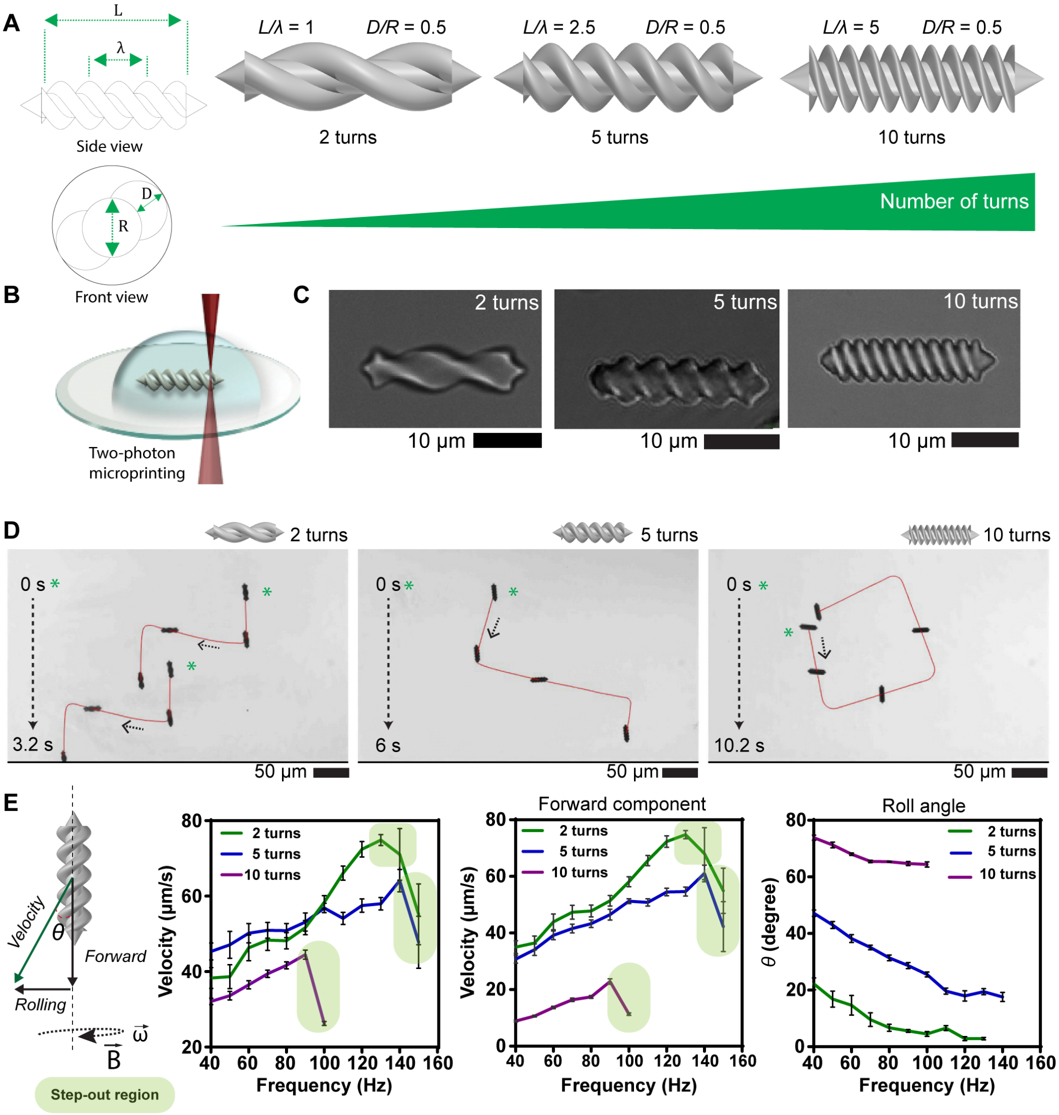

Fig. 1. Morphological design optimization for the swimming performance of the synthetic double-helical microswimmers. (**A**) Side- and front-view drawings of a microswimmer with design parameters. $L = 20$ μm, $R = 3$ μm, and $D = 1.5$ μm in all three designs. We varied the wavelength, λ, from 20 to 4 μm and selected the microswimmers with 2, 5, and 10 total turn numbers, $n = 2$ (double helix) × (L/ λ). (**B**) Illustration of the two-photon–mediated microprinting procedure of PEGDA ($M_n = 250$ Da). (**C**) Optical microscopy images of the 3D printed microswimmers. (**D**) Propulsion and steering of the microswimmers in PBS under the rotating magnetic fields (5-mT field strength) in assigned trajectories. Asterisk denotes the starting points, at $t = 0$ s. (**E**) The velocity vectors of the microswimmers with both forward and rolling velocity components. The frequency dependency of the velocity and roll angle showing the comparison of the locomotion performance of morphologically different microswimmers.

Whereas the immune system can present a highly dynamic and critical biological barrier for the safe execution of a microrobotic task, its impact on the design of medical microrobots has so far been overlooked. Microrobots, which are typically optimized for their high locomotion performance, usually have forms that are more complex than simple shapes such as spheres and rods (*4*). For swimming microrobots (i.e., microswimmers), locomotion at a low Reynolds number requires time-irreciprocal, asymmetric body movements (*12*), and capturing the fluid resistance acting on the entire body surface (*13*). However, the result of the interactions between these complex-shaped robot bodies with the cells of the immune system remains underexplored. Therefore, the interplay of the design parameters affecting both swimming performance and immunogenic behaviors should be better understood for a comprehensive approach to more efficient and safer in vivo functioning medical microrobotic system designs (*7*).

Here, we investigated the interactions of magnetically actuated and steerable helical microswimmers with immortalized macrophage cell lines and the primary white blood cells of freshly isolated mouse spleens, named splenocytes (Movie 1). Our focus was to understand the initial dynamics of the innate and adaptive immune responses that are affected by the morphology of the microswimmers. To this end, we systematically changed the helical turn numbers of the microswimmers and demonstrated the entangled relations among morphology, size, and surface chemistry of the microswimmers for eliciting differential immunogenic responses. Our findings suggest that structural design optimizations toward only enhancing locomotion performance can make the microswimmers immunogenic. Thus, this study suggests that structural optimization of the locomotion performance and immunogenicity should be considered simultaneously for any medical microrobot design. In addition, an understanding of morphology-dependent interactions between macrophages and microswimmers can introduce new engineering opportunities for biohybrid microrobot designs. In this direction, we introduce a biohybrid microrobot concept called immunobot (i.e., a magnetically actuated, biologically activated macrophage with an engulfed synthetic magnetic helical microswimmer) that combines the steerable and fast rotational mobility of synthetic microswimmers with the immunoregulatory and surface-crawling locomotion capability of macrophages for potential targeted immunotherapeutic applications in the future.

RESULTS

Structural design parameters of helical microswimmers for the best swimming performance

We previously proposed the design and computational fluid dynamics simulations of double-helical five-turn microswimmers with filled internal cores as concentrated cargo-carrying bodies (*14*). Here, we selected three morphological derivatives of the same design with the same body length ($L = 25$ μm), outer diameter ($R + 2D = 6$ μm), and body volume, only varying the number of helical turns along the major axis of the microswimmers, to investigate their interactions with the cells of the immune system (Fig. 1A and table S1). Two-turn and 10-turn microswimmers were chosen with lower and higher turn number counterparts of the 5-turn microswimmers. We microprinted these structures in three dimensions (3D) using two-photon polymerization from a prepolymer solution containing poly(ethylene glycol) diacrylate (PEGDA) and 3 weight % Irgacure 369 photoinitiator, as previously optimized (Fig. 1B) (*15*). Printed structures were magnetized by sputter-coating them with a 100-nm-thick nickel and then 50-nm-thick gold film, respectively, followed by a final surface modification with thiol-modified PEG. The final PEG modification aimed to minimize the unintended chemical interactions with the immune system, by means of the well-known shielding ability of PEG chains, and hence to dissect the impact of the structural effects on the immunogenic response (*16*). The structural fidelity of the printed final microswimmers is shown in Fig. 1C.

Rotational magnetic fields were applied to actuate and propel microswimmers by exerting torque around the helical axis (*17*, *18*). The helical microswimmers convert the rotational motion due to their asymmetric body shape to translational motion. Application of rotational magnetic fields with a custom-designed five-coil electromagnetic coil setup mounted on an inverted microscope enables the torque-based magnetic propulsion and steering of the microswimmers along assigned trajectories (Fig. 1D, fig. S1, and movie S1). The Reynolds numbers of the microswimmers are ranged between 10^{-4} and 10^{-5}, suggesting an inertia-neglected low Reynolds number regime during the locomotion.

Frequency-dependent swimming behaviors of the three helical microswimmers inside 1× phosphate-buffered saline (PBS) were compared until the magnetic torque was not able to overcome the resistive torque exerted by the fluid, i.e., until reaching their step-out frequencies. The step-out frequencies of the microswimmers were measured around 130, 140, and 90 Hz for 2-turn, 5-turn, and 10-turn microswimmers at 5-mT field strength, respectively (Fig. 1E). At frequencies lower than 100 Hz, 5-turn microswimmers outperformed the 2-turn and 10-turn microswimmers in terms of the swimming speed, in agreement with our predictions based on the computational fluid dynamics simulations (*14*). However, at frequencies higher than 100 Hz, 2-turn microswimmers began to move faster with a maximum mean speed of 74.9 ± 4.1 μm s^{-1} compared with 64.1 ± 5.2 μm s^{-1} and 44.5 ± 2.4 μm s^{-1} for the 5-turn and 10-turn microswimmers, respectively.

At lower rotational frequencies, rolling (drifting), defined by an angle θ between the forward velocity and the total velocity of the microswimmers, was common to all three microswimmers (Fig. 1E). This is because the microswimmers move close to the underneath solid boundary and an imbalance of the drag forces between the near-boundary and far-boundary parts on the microswimmers results in the rolling. As the frequency (and thus the forward velocity) increased, a decrease in the roll angle was observed. A structural comparison showed the lowest rolling with two-turn microswimmers across all swept frequencies, with a minimum 2.8° ± 1.2° of roll angle at the step-out frequency. However, the rolling angles at the step-out frequency were found to be 17.6° ± 2.8° and 64.7° ± 1.4° for the 5-turn and 10-turn microswimmers, respectively. The steeper decrease in the rolling angle of the 2-turn design is accounted for the increased forward velocity component at a faster rate compared with those of 5-turn and 10-turn designs.

In addition to the PBS solution, we characterized the swimming performance of the microswimmers inside whole fresh blood from a CD1 mouse. We observed a notable decrease in the step-out frequencies and the actuation frequency-dependent velocities in all groups compared with PBS due to the rate-dependent change in the blood viscosity and the fluidic drag exerted on the microswimmers (fig. S1 and movie S1). Nevertheless, we observed a similar behavioral pattern in the swimming characteristics as in the PBS solution. We measured the forward step-out velocity and the rolling angle of 2-turn microswimmers as 25.1 μm s^{-1} and 16.6°, respectively, which outperformed the 5-turn and 10-turn microswimmers with forward step-out velocities and rolling angles of 9.6 μm s^{-1}, 32.1° and 4.7 μm s^{-1}, 36.4°, respectively (fig. S1D). Considering the step-out swimming speed and the rolling properties, we ranked the locomotion performance of the swimmers as 2 turns > 5 turns > 10 turns in both PBS and whole blood.

Initial interactions of microswimmers with macrophages

To investigate the initial interactions of the microswimmers with a mouse peritoneal macrophage cell line, J774A-1, we first checked the cellular viability in the first 24 hours of exposure. The viability of cells was found comparable among all microswimmer groups and with the bare tissue culture plate, indicating that no toxic interactions were evident for the macrophages in the presence of the microswimmers (fig. S2). We next examined the physical interactions of macrophages with the microswimmers using scanning electron microscopy (SEM), bright-field optical microscopy, and confocal microscopy. To closely monitor how macrophages approach to the microswimmers, probe their surfaces, orient themselves, and muster the adequate force to eventually complete the phagocytosis processes, we elevated the stringency to the engulfment condition by exposing them to the surface-bound microswimmers, as printed on the glass substrate.

The SEM images showed the actin protein–based membrane protrusions of filopodia and lamellipodia interacting with the body of the five-turn microswimmers (fig. S3). Finger-like filopodia protruded from lamellipodia for probing the environment from a distance and for pulling potential targets toward the cell body by acting like a tentacle to facilitate the phagocytosis process (fig. S3, B and C). Filopodia generated by macrophages can exert tensile forces up to several hundred piconewtons (*19*). Filopodia also influence cellular decisions to extend lamellipodia, which are the leading edges of the cell and generate much higher forces needed for phagocytosis and cellular mobility. Macrophages used lamellipodia to flatten over the surface of microswimmers to wrap them completely for internalization (fig. S3D).

To better investigate filopodia and lamellipodia during the phagocytosis, we tracked the time-lapse images of over 1200 macrophage-microswimmer interactions. The microswimmers are not expected to release endotoxins or other chemicals that could recruit macrophages; the only way for them to find the microswimmers was the physical interactions as a result of the random encounters during probing the environment. The physical interactions could therefore

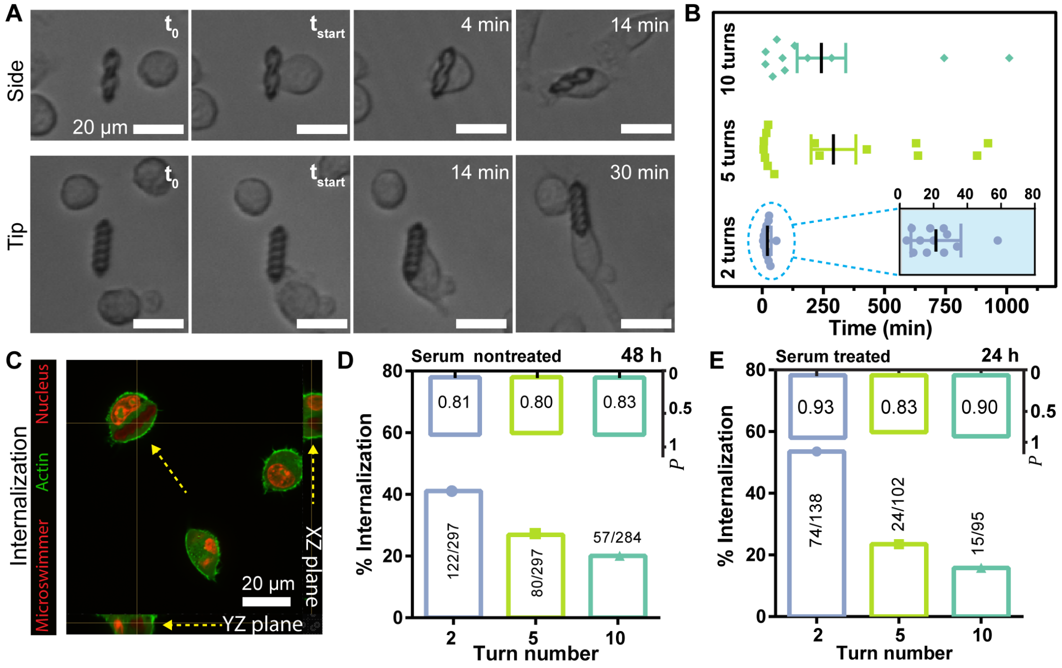

Fig. 2. Phagocytic interactions of macrophages with the helical microswimmers. (**A**) Snapshots of the macrophages. At t_0, macrophages stochastically probe their environment and, at t_{start}, encounter microswimmers from any directions to start wrapping, followed by detachment, reorientation, and internalization. (**B**) The elapsed time of the complete internalization of microswimmers after t_{start}. Inset shows the internalization time distribution for the two-turn microswimmers. (**C**) The sectional view of a confocal image verifying a completely internalized microswimmer in a macrophage at 48 hours. (**D** and **E**) Comparison of the numbers of completely internalized microswimmers with respect to the total numbers of microswimmers investigated under comparable random encounter probabilities (*P*). In columns, the percentage of internalization rates represented as number of completely internalized microswimmers over total number of microswimmers. (D) Microswimmers without any pretreatment. (E) A priori 4-hour serum treatment to the microswimmers before introducing macrophages.

be initiated from any orientation with respect to the long axis of the microswimmers (Fig. 2A, fig. S4, and movie S2). After the first contact, the complete internalization took place in the sequence of flattening over the microswimmer surface, forceful detachment from the substrate, and reorientation for favorable engulfment. After the detachment, macrophages could change the position and orientation of the microswimmers in 3D to better facilitate the internalization (fig. S4B).

When the phagocytosis process was completed and the microswimmer was inside the cell, we observed a stable orientation angle inside the phagosomes. When we compared it with the microswimmers that were initially detached, we observed a similar dynamic adjustment in the orientation, with the long axis pointing toward the cell to facilitate the phagocytosis process (fig. S4C). This observation is in alignment with the previously demonstrated internalization of the rod-shaped micron-scale preys (*20*). The elapsed time of phagocytosis for 2-turn microswimmers, i.e., from the beginning of the physical contact until the time of complete internalization, was 20 min on average (Fig. 2B), whereas the internalization took notably longer time, around 4 hours on average, for 5-turn and 10-turn microswimmers. The variances in the phagocytosis time among the same group of microswimmers and between microswimmer groups with different turn numbers were due to the initial orientation angles that limited the kinetics of flattening over the microswimmer surface. We will refer to these morphology-oriented discussions in the following section again. After the successful phagocytosis, the macrophages were still able to crawl with their internal cargo (movie S2).

To extend our observations, we further stained the actin cytoskeletons and the nuclei of the cells for fluorescence imaging and acquired confocal z-stacks to define the internalization status (Fig. 2C). Complementing our similar observations earlier, the initiation of the physical contact began with filopodia and lamellipodia protruding along the cover glass surface and penetrating in the underneath grooves to wrap the microswimmers and establish a grip (fig. S5). We observed actin fiber enrichment, evidenced by the increase in the fluorescence intensity, at the point of interaction with the microswimmers, a formation called the phagocytic cup, which initiates and drives phagocytosis (figs. S5 and S6A) (*21*). The phagocytic cups were developed around the accessible circumference, starting from the underneath of the helical geometries and conforming inside the grooves (fig. S5). We observed phagocytic cup formations in all three groups of microswimmers that accompanied the internalization process. Once the internalization was complete, the phagocytic cup formation disappeared and the microswimmers were entrapped inside phagosomes (Fig. 2C and fig. S5B).

Next, we compared the internalization rates of the microswimmers in certain time intervals. For this, we needed to ensure the validity of the comparative analyses between the microswimmer groups by ruling out extrinsic factors that can arise repeatability problems, such as fluctuations in local cell and microswimmer densities in each experiment (fig. S6C). Therefore, we calculated random encounter probabilities (*P*), which is defined as the probabilistic occurrence of the random event that a macrophage physically encounters a microswimmer in that particular experiment. We always investigated a large number of microswimmer-macrophage interactions to ensure that there were comparable *P* values in each microswimmer group with different turn numbers. When macrophages interacted with comparable *P* values, the complete internalization rates of microswimmers at 24 hours were sorted as 1.6, 4, and 0% internalization for the 2-turn, 5-turn, and 10-turn microswimmers, respectively. We ascribed this to the effective shielding by PEG. By the end of 48 hours, however, the internalization rates were sorted as 41, 27, and 20% (Fig. 2D and table S2). The accelerated internalization rates in the second 24-hour period can be attributed to the serum proteins adsorbed on the microswimmer surface, thereby creating a thin macromolecular corona facilitating the recognition

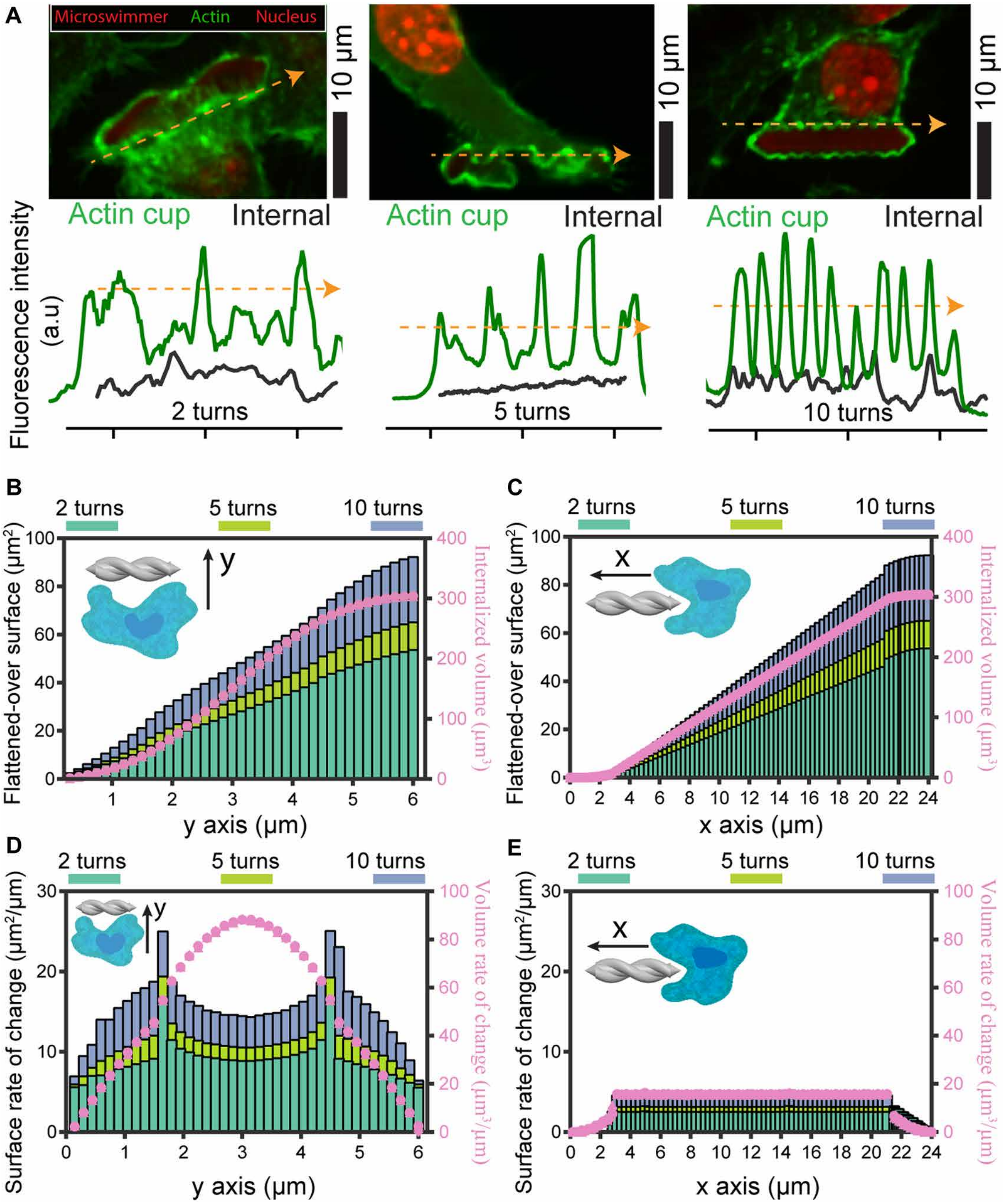

Fig. 3. The internalization dynamics of the helical microswimmers. (**A**) Macrophages extending their membranes to completely flatten over the microswimmers. The presence of an actin cup indicates an active engulfment process that entails increased surface created by the macrophage due to flattening and increased volume occupied within the macrophage. The interplay of the costs generated by the created new macrophage surface around the microswimmers and the occupied microswimmer volume determines the kinetics and the dynamics of the internalization. a.u., arbitrary units. (**B**) The estimated new volume and surface that need to be created by macrophages as they internalize microswimmers along the directions perpendicular (from the side) and (**C**) parallel (from the tip) to the helical axis. (**D** and **E**) The rate of change of volume and surface increases during the internalization from the side and tip of the microswimmers.

by the macrophages (*22*). To test this, we pretreated the microswimmers with 100% fetal bovine serum (FBS) for 4 hours before introducing macrophages. The internalization trend remained the same yet became more pronounced as early as 24 hours with complete internalization rates of 53, 23.5, and 15.8% for 2-turn, 5-turn, and 10-turn microswimmers, respectively (Fig. 2E and table S3). As a result, the macromolecular corona formation on the microswimmer surface can be a distinct factor for the microswimmer-macrophage interactions and hence may require a follow-up investigation including different physiological fluids with different proteinaceous contents.

Morphology-dependent evolution dynamics of phagocytosis

We attempted to understand the disparity in the internalization rates of the microswimmers with different turn numbers by considering parameters related to their surface area, volume, and their rate of changes depending on their initial contact orientations, as discussed in the earlier section (Fig. 2A). Following the propagation of actin waves can be a useful tool to determine the interacting surface area to be engulfed (*21*). To this end, we considered the propagation of the phagocytic cups that flatten over the microswimmers and conform to their helical grooves, which maximize the contact area and hence the applied pulling force (Fig. 3A). This process requires the formation of a new membrane and its deformation on the helical geometry, which presents both energy and material costs.

Interpreting the dynamics of phagocytosis in the frame of morphology-dependent energy cost was suggested in the previous theoretical studies, where the phagocytosis of spiral pathogens requires higher energy compared with the spherical ones due to the presence of curvature regions of the spiral structures (*23*–*25*). In this view, we realized that the average projection area of a cell flattened over the microswimmer surface increased above 2000 μm^2, compared with the average projection area of an idle macrophage of around 250 μm^2 (fig. S7). This suggests almost an order of magnitude increase in the surface area. Hence, the phagocytosis could be completed only if enough new membrane is supplied. As a result, the interacting surface area and its rate of change along the direction of propagation of the phagocytic cups are critical for the completion of the internalization process.

The volume of a microscopic object is also an important discouraging factor for the macrophage because the larger the volume is, the larger the macrophage should grow its own volume to accommodate the object. This results in an increased cost of energy and cellular building resources, such as the membrane and adequate space for the existing cytoplasmic subcellular components.

Because of the random encounter, the statistical stochasticity of the direction of the macrophages to start the internalization of the microswimmers will be the same regardless of the turn number (Fig. 2A). For this reason, we looked into the amount of volume and surface area that need to be engulfed as the phagocytic cup propagates through a microswimmer, either from the side or from the tip, until the internalization is complete (Fig. 3, B to E). When a macrophage began the internalization from the tip, progression of the contact surface area, the engulfed volume, the area rate of change, and the engulfed volume rate of change remained lower compared with the scenario when it began from the side. As a result, the cost of internalization for 1-μm-distance propagation of the phagocytic cup along the helical axis becomes lower than the cost of propagation along the perpendicular axis. This explains the reorientation of the microswimmers after their detachment from the surface, so the tip of the microswimmers tended to point inward of the cell during the internalization.

When we compared the microswimmers with different turn numbers, both the amount of volume and the volume rate of change that the macrophages need to internalize remain the same along the same axes. This shows that the stress induced by the internalization of the volume applies comparably for each microswimmer with different turn numbers. However, both the surface area and the area rate of change increase substantially as the turn number increases in both axes (10 turns > 5 turns > 2 turns). It suggests that flattening over 10 turns is more difficult for the macrophages and, thus, energetically becomes more costly than flattening over 5 and 2 turns. The surface cost trend is consistent with the internalization trends (2 turns > 5 turns > 10 turns) because the least costly 2-turn microswimmers are the easiest to internalize.

The impact of the filopodia and the contact area on the rate of phagocytosis is better pronounced when we systematically change the size of the microswimmers. Previous research suggested that the size-dependent difference in the internalization rate of the simple objects, such as spheres and rods, originated from the attachment of membrane ruffles to the objects. Microspheres with a certain intermediate size were found to make better contacts with the membrane ruffles than the smaller and larger ones, which had a profound impact on phagocytosis (*26*). Similarly, we tested the impact of the swimmer size on the internalization rate by changing the length of the microswimmers from 10 to 40 μm while preserving all the aspect ratios. By doing so, we were able to change the microswimmer volume by 256-folds (fig. S8, A and B). When the size of the helical grooves of the microswimmers was sufficiently large, the filopodia were able to extend into the grooves to form the phagocytic cups. In these grooves, we observed the highest actin polymerization, indicating better contact and higher pulling forces to the microswimmers (fig. S5). As a result of this dominant effect against the volume cost, we observed the highest internalization rate for the microswimmers with 25-μm length (fig. S8C).

As the depth of the helical grooves in the 10-μm-length microswimmers shrank down to a few hundred nanometers (table S4), the macrophages lost their ability to extend into the grooves, and the contact area with the microswimmers for pulling was lower. Thus, cells spread on the 10-μm-length microswimmers without successful internalization (fig. S8D). As a result, 25-μm-length microswimmers with 15.6-fold volumes were internalized at a higher rate compared with 10-μm-length swimmers. Nevertheless, as the size of the swimmers grew larger than 25 μm, we observed that the volume effect began to dominate, and the internalization rate went lower. We observed that 40-μm-length microswimmers were predominantly internalized by the formation of multinuclear giant cells (fig. S8E). These giant cells are fused multinucleated macrophages to internalize larger intruders that cannot be engulfed by a single macrophage (*27*). Although giant cells were dominant in the internalization of 40-μm-length microswimmers, we observed giant cells in all microswimmer groups with a lower abundance (fig. S8F).

Given the discussion above for the size dependency, when we compared the size-dependent internalization rates of two-turn and five-turn microswimmers, the impact of the surface morphology and volume did not proportionally distribute on each design. The groove size change in the two-turn microswimmers is less pronounced than for the five-turn microswimmers because the wavelength of the two-turn microswimmers is larger (table S4). This explains the disproportional change in the internalization rates as a function of size for both designs. Both designs, however, followed similar size dependency patterns with the highest internalization rates at 25 μm in length. Furthermore, two-turn microswimmers tended to be internalized faster than five-turn microswimmers across all lengths. These results show that there is a complex entanglement of morphological features and size parameters governing the internalization process.

Differential immunogenic response based on the structural parameters of the helical swimmers

Next, we investigated the immunogenicity of the microswimmers in the presence of freshly isolated primary mouse spleen cells, called splenocytes (Fig. 4A). These cells consist of a variety of white blood cell populations, such as macrophages and T and B lymphocytes. Compared with a macrophage cell line, the use of freshly isolated primary cell pools with both nonspecific and specific immune cells will provide a better representation concerning the interactions between the microswimmers and the immune system as a complex combination. We introduced the spleen cells to the surface-bound microswimmer arrays for a period of 96 hours and acquired images every 24 hours to compare the temporal interactions (figs. S9 to S11). We observed that splenocytes exposed to all three microswimmer groups exhibited comparable viability and proliferation in 72 hours to those that were not exposed to the microswimmers (Fig. 4B and fig. S12). The initial immunogenic response of the cells became evident under the microscope at 48 hours when cells started accumulating around the microswimmers (figs. S10 and S11). Because the bright-field imaging fails to conclude the internalization status of the microswimmers in a conclusive way, we chemically fixed the cells at 96 hours, so we were able to freeze the final interactions of cells with the microswimmers to closely monitor the phagocytic interactions with the splenocytes. We observed a heterogeneous population of cells around the microswimmers formed a cluster.

Macrophages were distinguished from their phagocytic cups around the microswimmers. During the macrophage engagement with the microswimmers, we observed that macrophages were physically interacting with T and B lymphocytes (figs. S13 and S14).

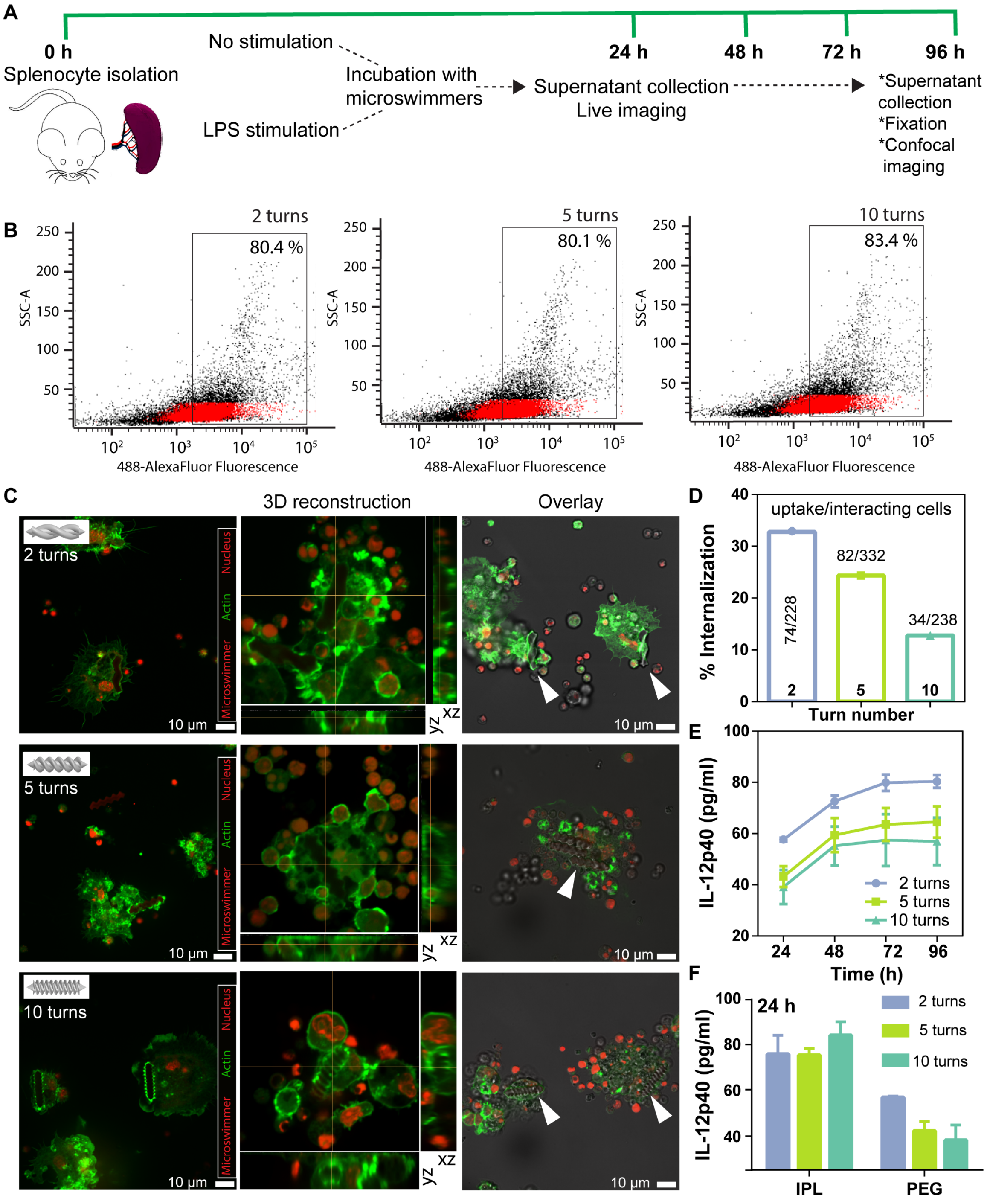

Fig. 4. Primary immune cell response to the synthetic microswimmers. (**A**) Experimental workflow for coincubation of splenocytes freshly isolated from mouse spleen. SSC-A, side scatter. (**B**) Fluorescence-activated cell sorting analysis showing the proliferation rates of the splenocytes at 72 hours. (**C**) Confocal images of the LPS-stimulated splenocytes at 96 hours. Lymphocytes around the spread macrophages are also evident. (**D**) The percentage of internalization rates of the microswimmers by LPS-stimulated splenocytes at 96 hours. Data represented as total uptake over total interacting cells. (**E**) IL-12 p40 in the culture supernatant, secreted from the splenocytes in response to microswimmers, detected by enzyme-linked immunosorbent assay. (**F**) IL-12p40 release in response to microswimmers made from commercial photoresist, IPL, and PEG at 24 hours.

T and B lymphocytes could be differentiated by their round cellular morphology and large nucleus size compared with their little cytoplasmic space as shown in Fig. 4C. In the body, the cells of the nonspecific immune system, such as macrophages and dendritic cells, internalize the foreign intruder and release proinflammatory signals to recruit the cells of the specific immune system, such as T and B lymphocytes. T and B lymphocytes are then trained by the macrophages and dendritic cells to launch a more effective specific immune reaction. As a result, the accumulation of the T and B cells around the macrophages during the internalization of the microswimmers suggests that a specific immune response was underway against the microswimmers.

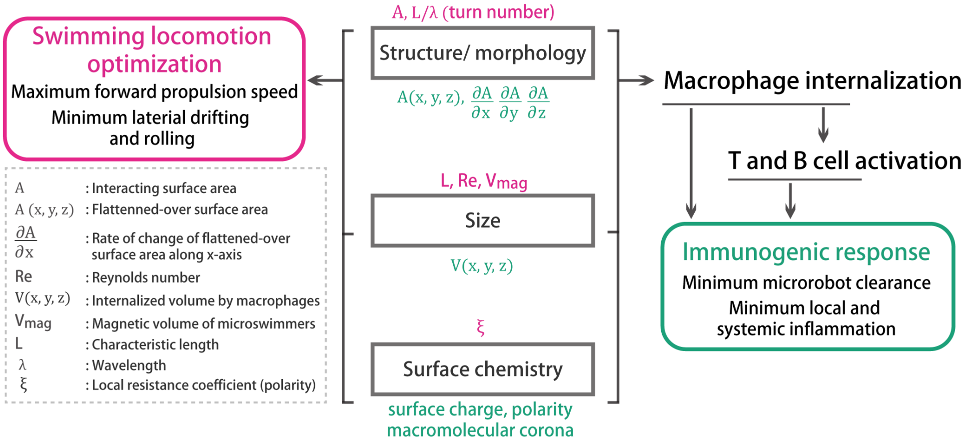

Fig. 5. Microrobot design parameters influencing both locomotion and immunogenic behavior together. In the case of a helical microswimmer design, given entangled design parameters need to be selected correctly for maximizing the robot's locomotion performance while minimizing its immunogenic response.

The phagocytic interactions of microswimmers with splenocytes followed a pattern similar to the interactions with macrophages (Fig. 4D and table S5). In a pathological environment where microrobots would operate, the immune cells would not be in their quiescent states; instead, it is highly likely that the microswimmers will find a microenvironment in which the immune cells have been activated. One such stimulant is called bacterial lipopolysaccharides (LPSs), which stimulate an immune response by interacting with the surface receptor CD14 on macrophages, which subsequently results in the secretion of proinflammatory cytokines (*28*). We observed that the LPS-activated splenocytes caused a higher proliferation rate of the cells, and cells started to form clusters, which were evident in the microscopy images (figs. S10 and S11). The proinflammatory cytokine interleukin-12 p40 (IL-12p40) release by the activated macrophages in splenocytes was similar to the internalization results with higher response against two-turn microswimmers (Fig. 4E). We also tested the reaction of the splenocytes toward the change of the base material by fabricating the microswimmers from commercial photoresist (IPL-780). Turning the base material to plain IPL without any further treatment did not show the same turn number–dependent proinflammatory IL-12 release (Fig. 4F). However, the comparison between the PEG-based and IPL-based microswimmers revealed the increased IL-12p40 response against the commercial resin. In these designs, both morphology and surface chemistry play confounding roles on the elevated IL-12 levels. Considering the surface area ranking (10 turns > 5 turns > 2 turns), macrophages might have been exposed to the highest immunogenic chemicals on the IPL-based 10-turn swimmers and the lowest immunogenic chemicals on 2-turn swimmers. This could explain the compensation of the morphology-related effects, where the surface chemistry becomes a dominant factor. These results show that the use of PEG backbone material reduced the potential immune response by macrophages as supporting evidence of our initial design claims.

Concerning the microrobot locomotion performance, two-turn microswimmers exhibited the highest swimming performance due to their hydrodynamic design. However, we found that 2-turn microswimmers were also more immunogenic compared with 5-turn and 10-turn microswimmers. Although 10-turn microswimmers proved the less immunogenic, their swimming performance was markedly lower compared with 2-turn and 5-turn microswimmers. Depending on the immunological activity at the site of application, structural optimizations may be used in favor of the swimming speed over the anticipated interactions with the immune cells. In the body, there are immune-privileged sites, such as the central nervous system and eye, where the immunological activity is lower than the rest of the body. In these areas, two-turn microswimmer may be more advantageous considering its higher speed. However, in a body site where massive interactions with immune cells are expected, there may be a design compromise to choose a structure with lower speed, such as 10-turn, for gaining more invisibility to the immune system. If a compromise is needed on both sides, then five-turn emerges as an in-between alternative. Although coating with a passivating surface, such as erythrocyte membrane, is also useful for immune evasiveness, the morphology of the microswimmer may play an especially important role when we want to use the volume of the microswimmer to release a diagnostic or therapeutic agent. Coating the microswimmer surface could hamper the access of therapeutic moieties to the target tissue, and thus morphology-dependent immune evasiveness becomes critical to enable the therapeutic outcome.

Entanglement of the microrobot design parameters influencing both swimming and immunogenic behaviors

We show that the surface morphology, chemistry, and size of a microswimmer can markedly influence the outcome of the interactions with the cells of the immune system (Fig. 5). A safe microrobot design therefore relies on the optimization of these major parameters, which should aim to maximize the locomotion performance and to minimize the early interactions with macrophages. Minimization of the physical interactions with macrophages or slowing down the internalization process can lower the deployment of the specific immune system for a more extensive immunogenic response.

From the swimmer design point of view for the low Reynolds number regime, the surface morphology determines the coupling between the magnetic torque applied to the microswimmer and the fluid resistance acting on the swimmer surface for the rotational-to-translational transfer of the motion. From the immunogenicity point of view, the surface morphology determines the costs of the total surface area to be internalized and the rate of change in the surface area as the macrophage continues its flattening over. We show that favoring both parameters can lower the immunogenicity. Macrophages also use topographical features, such as grooves, to enrich actin polymerization for exerting higher pulling forces. As a result, avoiding redundant surface topographies could improve the immunogenic outcome.

Taking into account the microrobot surface chemistry is also imperative for both its locomotion performance and its immunogenicity. Helical microswimmers with hydrophobic surfaces exhibit larger step-out frequencies and higher maximum forward velocities compared with their hydrophilic counterparts (*13*). In terms of immunogenicity, surface chemistry determines the content of the spontaneously formed macromolecular corona on the surface of materials and microrobots (*29*). The corona can induce an immune response against the microswimmers either by giving a new biological identity to the microswimmers to be recognized by the macrophages or by triggering the biophysical process of protein misfolding and aggregation, which also leads elimination of the microrobots from the body. The function of macrophages depends on the initial physical interaction and chemical engagement with their target to differentiate native from foreign. In this regard, surface chemistry remodels such interactions through macromolecular corona in favor of either immune reaction or no action at all. We demonstrated that the formation of macromolecular corona when microswimmers were pretreated with FBS induced an accelerated immune response against the microswimmers (Fig. 2E). In addition, dissimilar proinflammatory cytokine release against the microswimmers, which have the same structural properties but different surface chemistries (PEG and IPL), reveals the differential surface chemistry effect on inducing the immune response (Fig. 4F).

The impact of the microswimmer size on the macrophage phagocytosis is nontrivial and highly entangled with the surface morphology. When the microswimmer is small enough that a single macrophage can accommodate it, the favoring impact of the surface morphology can surpass the volumetric cost for the internalization. However, when the size becomes larger than a single macrophage can internalize, giant cells plays a major role in the internalization. The dynamics of this formation require more elaboration; however, we observed that this seems to be a dynamic process, and the cells can divide and the resulting daughter cells fuse to form a binucleated cell, consistent with the previous works on phagocytosis of long asbestos fibers by macrophages (*30*). From the microrobotics perspective, although the swimming speed is proportional with the characteristic length scale, the size of the microrobot is determined by the expected medical function and the anatomical demands of the sensitive pathology where it can make a disruptive impact.

Here, our double-helix microswimmer design is fully rigid. A largely deforming soft or compliant swimmer or robot body may exhibit a markedly different behavior under the flattening of macrophage phagocytosis. To this end, soft microswimmers relying on undulating body movements could be a very interesting example to study in the future (*31*), where their interaction with the cells of the immune system could be more dynamic and more resistant to internalization than our observations with the microswimmers with a rigid body and complex 3D morphology.

Controlled microswimmer-immune cell interactions enabling alternative biohybrid immunobot design strategies

A biohybrid microrobot design physically integrates a live microorganism with a nonliving body to exploit the microorganism's inherent machinery of coupled actuation, sensing, and locomotion by harnessing the biological fuels in the living environment to perform tasks, such as manipulation, targeting, and cargo delivery (*6*, *32*, *33*). Biohybrid microrobot designs have exploited bacteria, algae, or sperm as the active living components for locomotion and sensing, and the synthetic parts have been the passive functional materials (*34*–*36*). The propensity of internalization of the helical microswimmers can be exploited to realize alternative biohybrid robot design approaches by hybridizing synthetic swimmers with macrophages. This could give an opportunity of combining the separately superior parts of the synthetic and biohybrid microrobots in an immunobot for future targeted immunotherapeutic applications. In such an application, the immunobot may be navigated long distances using magnetic fields that actuate the synthetic microswimmer component, and self-propelled autonomous crawling locomotion of the live macrophage may be used for sensing-coupled fine-tuned localization or tissue penetration (Fig. 6, A, B, and E). The release of proinflammatory cytokines from the immunobot may recruit the other cells of the immune system to generate a local inflammation.

To explore such a biohybrid robot design method and to achieve the internalization, we added the magnetic microswimmers to the cell culture, so their uptake could be accelerated without requiring prior detachment from the surface (Fig. 6A). When these microswimmers were internalized, the macrophages were not able to degrade them, at least in the time scale of several days, providing an opportunity for long-run robotic task execution. The rotating magnetic fields enabled the rolling of the macrophages on the substrate surface, around, and over the cells (Fig. 6, B and C, and movie S3). On the glass substrate, the average rolling velocity of the immunobots, where the microswimmers were completely internalized, was around 2.8 mm min^{-1} under 5-mT rotating magnetic field with 12-Hz excitation frequency. The immunobots behaved differently when they were moving around and over the cells under the same actuation conditions. Immunobots slowed near the cells for short durations (varying between 0.5 and 4 s), followed by sudden velocity jumps up 600 μm min^{-1} (Fig. 6B and movie S3). Such velocity jumps were not observed when the immunobots were moving on the plain glass substrate. A similar observation with enhanced translational velocity was recently reported with microparticles propelled on surfaces with microtopographies (*37*). In our experimental design, adherent cells created a topography on the surface for the rolling microswimmers, which resulted in a similar observation. The observed phenomenon of the instantaneous velocity jumps could also be affected by the repulsive interactions between the cells by virtue of negatively charged cellular membranes. This observation could be applied for overcoming the generic problems of spontaneous and nonspecific attachment of synthetic microswimmers to the cells they were carrying and in the surrounding environment (*38*). Microswimmers have been greatly affected by this problem, which remains a grand challenge that hinders the future potential in vivo free-swimming performance of such designs. The immunobot design demonstrated the capability of uninterrupted locomotion in the prescribed trajectories regardless of the cells residing along their pathway, whereas the individual microswimmers failed to do so (movie S5).

In the second design type, we demonstrated the actuation of partially interacting two-turn microswimmers that remained attached to the outer membranes of the macrophages. Under the rotating magnetic field of 10-mT magnetic field strength and 10-Hz excitation frequency, these immunobots exhibited a rowing type of motion (fig. S15). Cells were not able to complete the rolling; instead, the microswimmer attached to the cell membrane did consecutive forward and backward movements, during which the immunobot always moved in the forward direction (fig. S15). The velocity of the immunobot

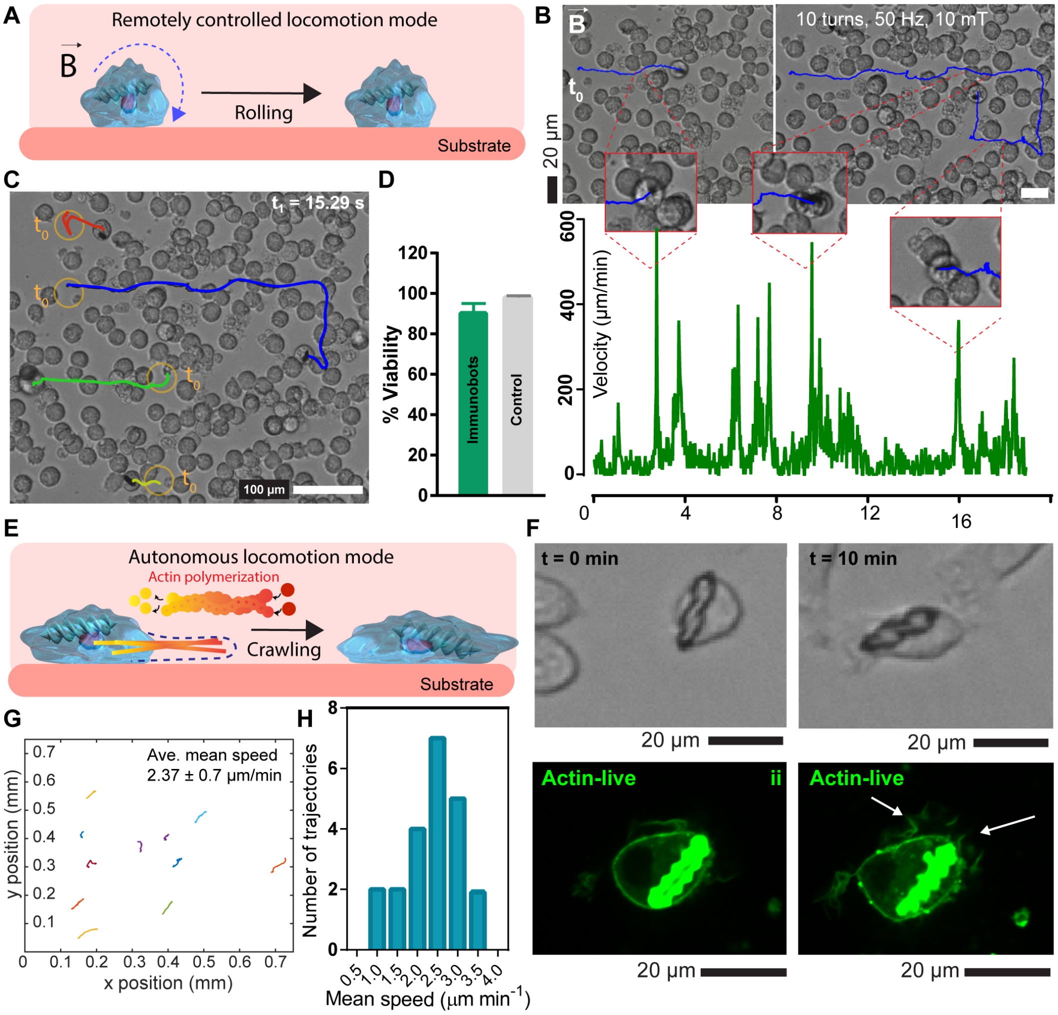

Fig. 6. Biohybrid immunobot design bringing together a macrophage with a synthetic microswimmer to enable bimodal locomotion capability in a biological environment. (**A**) Illustration of the surface roller immunobot achieved by the magnetic torque–based actuation and (**B**) steering of an immunobot around and on top of the semiadherent nonmagnetic macrophages. Increases in the instantaneous velocities were observed as the immunobot propelled on top of the adherent nonmagnetic macrophages (insets corresponding to peaks). (**C**) Tracking of multiple immunobots in roller mode actuated simultaneously. Orange circles denoting the initial positions of the immunobots at t_0. (**D**) Viability of the immunobots compared with control cells at 72 hours. (**E**) Illustration of an immunobot in the autonomous (crawling) locomotion mode by the intrinsic dynamic reorganization of the actin cytoskeleton. (**F**) Snapshots of the time-lapse recordings during motion. Fluorescence images showing live actin protrusions during the crawling. (**G**) 2D displacement trajectories of the immunobots displaying crawling locomotion with an average speed of 2.4 ± 0.5 μm min^{-1}. (**H**) Mean speed distribution of the crawling immunobots.

oscillated between 6.5 and 1.3 mm min^{-1} due to this rowing type of motion (movie S3). In addition, we demonstrated that the viability of immunobots was comparable with the bare macrophages after 72 hours (Fig. 6D), showing the nontoxicity of the microswimmers to the macrophages within this time window.

In both design types, the externally applied magnetic field could drive the locomotion of the immunobots long distances. In addition, we demonstrated that the self-propelled autonomous movement of the macrophages could drive the locomotion of immunobots short distances (Fig. 6E). The actin cytoskeleton is the primary and essential coordinator of this process, transmitting the generated force to the substrate and recycling it when necessary for the crawling type of locomotion (*39*). In addition, macrophage-based immunobots can penetrate the tissues by overcoming cell-gated barriers, which require specific cell-cell interactions (*40*). To overcome such cell-cell connections, a rupture force at least on the order of 200 nN is required (*41*). Synthetic microswimmers the size of around 20 μm can exert forces on the order of 20 pN (*42*). Therefore, the immunobot design scheme can provide a temporary or semipermanent means to move in the solid body sites, which has not succeeded yet. To characterize our immunobot designs, we investigated the autonomous crawling and the involvement of the actin cytoskeleton (Fig. 6F). The mean crawling speed of the macrophages did not change in the biohybrid construct (2.4 ± 0.5 μm min^{-1}) compared with their free nonhybrid forms (4.1 ± 2.2 μm min^{-1}) (Fig. 6, G and H, and fig. S16). The capability of both remote magnetic actuation and switch to the biological autonomous self-propulsion mode of locomotion can be controlled depending on the biological conditions and the desired application. As opposed to bacterial and algal biohybrid microswimmers, macrophage-based cellular cyborgs have more potential to overcome the immunological barrier through design of personalized microrobotic systems using patients' immune cells. Previously, therapeutic stem cells and several leukocyte types were loaded with magnetic nanoparticles to steer them in the body for cell-based therapies (*43*–*47*). Notwithstanding, standardizing these protocols has been challenging because of the inhomogeneity in the loading amounts of nanoparticles to each cell. The increased doses of free nanoparticles inside the cells to efficiently steer them could also cause acute or accumulation-related cell toxicities (*48*). By forming a biohybrid with a structured micromagnet, we were able to impart homogenous magnetization to each cell and keep them compartmentalized, reminiscent of an artificial organelle. In addition, the present study reports the controlled locomotion of cells by torque-based motions, which presents a more effective route compared with those offered by gradient-based pulling.

DISCUSSION

The present study used helical microswimmers as model designs to systematically investigate the entanglement of the microrobot design parameters—including surface morphology, chemistry, and size—in affecting both locomotion and immunogenicity at the same time (Fig. 5). We demonstrated that although the three microswimmer groups have the same length, width, volume, and volume rate of change along the axes of macrophage phagocytosis, the variation of surface area and its rate of change along the axes of macrophage phagocytosis played a dominant role in the differential immunogenicity of the microswimmers. Therefore, the two-turn microswimmers, which exhibited the best locomotion performance, at the same time ended up being the most immunogenic. We showed that the interaction of the complex 3D morphology of the microswimmers with the macrophages can result in counterintuitive responses. Whereas the internalization rate of simple geometric structures is reversely proportional to their size, the surface morphology and the presence of contact features with comparable sizes of the cellular filopodia can markedly change the outcome. For the microswimmers larger than a single macrophage can accommodate, multinuclear giant cells form as a response. The surface chemistry and its interaction with the macromolecules in the physiological environment can significantly affect the immunogenicity, as we presented the impact of the macromolecular corona on the accelerated internalization of the microswimmers. Understanding the scope and extent of the interaction dynamics between the microswimmer body and the immune system is crucial for the addressing potential safety issues associated with in vivo medical microrobots. Therefore, the present study provides a perspective on the rational design of high-performance microswimmers to reduce potential uncontrolled immunogenicity and, thereby, to achieve the desired functional (e.g., therapeutic) benefits with minimum overall compromise. The ranges of structural complexity, material diversity, and size of the already developed microrobotic designs are larger than what could be explored herein, but the presented mechanistic and methodologic principles can still apply to explore them and other future microrobot designs.

The exploitation of the interactions of synthetic microswimmers with macrophages can also enable new types of biohybrid microrobot designs (immunobots), where both biological autonomous and remote torque-based locomotion modes could be realized in a single microrobot. We show such a proof-of-concept immunobot design demonstrating the capability of overcoming the adhesion problem of the synthetic microswimmers to surrounding cells by uninterrupted fast and steerable rotational surface locomotion whereas the individual microswimmers failed due to non-specific adhesion to the cells. Such a biohybrid design strategy—unifying the steerable and fast rotational mobility of synthetic microswimmers with the immunoregulatory and autonomous infiltration capability of macrophages—could enable future medical microrobots for immunotherapeutic applications. A controlled immune response elicited using such biohybrid systems may be directed toward tumors by steering the microrobots to the vicinity of the tumors, potentially confining the effect of the immune response around the tumor. However, for such future in vivo immunobots to be realized, the internalized magnetic structure shape, size, surface chemistry, and anchoring need to be optimized further to achieve optimal magnetically actuated locomotion performance and immunotherapeutic functions. In addition, our immunobot approach may pave the way for developing fully nonimmunogenic, personalized biohybrid microrobots using the patient's own macrophages in the future.

MATERIALS AND METHODS

The materials used in this study were obtained from Sigma-Aldrich unless otherwise mentioned. The materials were used as received without any further purification. A detailed description of the methods is available in the Supplementary Materials or can be accessed from the authors.

Fabrication of the microswimmers

The computer-aided designs of the microswimmer bodies were 3D-printed using a two-photon–based direct laser writing system (Photonic Professional, Nanoscribe GmbH) equipped with a 63× oil-immersion objective (numerical aperture, 1.4). Laser power and galvanometric mirror *x* and *y* scanning speeds were optimized for printing as 20 mW and 1.5×10^5 μm s^{-1}, respectively. For the final surface modification with PEG, gold-sputtered microswimmers were initially cleaned using an ultraviolet ozone cleaner for 20 min, followed by reacting with a sulfhydryl derivative of PEG, 10-kDa mPEG-SH (Laysan Bio, Arab, AL), for 2 hours in ultrapure water H_2O.

Cell culture and imaging

Primary splenocytes were isolated from fresh spleens obtained from C57BL/6. Cells were incubated in RPMI 1640 medium supplemented with 10% (v/v) FBS (Gibco), penicillin (50 UI ml^{-1}), and streptomycin (50 μg ml^{-1}) in a humidified, 37°C, 5% CO_2 environment. For the experiments, cells were seeded at a density of 1×10^6 cells ml^{-1} (2×10^6 cells per group). For the LPS stimulation, the cells in the respective groups were treated with LPS (10 μg ml^{-1}). Mouse peritoneal macrophage cells, J774A-1 (ATCC TIB-67), were cultured in Dulbecco's modified Eagle's medium supplemented with 10% (v/v) FBS, penicillin (50 UI ml^{-1}), and streptomycin (50 μg ml^{-1}) in a humidified, 37°C, 5% CO_2 environment using 75-cm^2 polystyrene cell culture flasks. Cells were used at passage numbers lower than 5, and surface detachment during splitting was performed using a cell scraper when they reached 80% confluence. For the experiments, the cells were seeded at a density of 1.5×10^5 cells per group. Serum treatment was performed by incubating microswimmers in FBS for 4 hours at 37°C, followed by washing with a growth medium. Live-cell time-lapse images (1 frame min^{-1}) were acquired in the bright-field mode of an inverted microscope from Nikon Instruments Inc., Eclipse Ti-E equipped with an environment chamber for the control of physiological conditions. For confocal microscopy, the cells were fixed in a formaldehyde solution [2.5% (v/v) in PBS] for 25 min and permeabilized in Triton X-100 [0.1% (v/v) in PBS] for 10 min. After washing the cells with PBS, cells were stained in a solution containing Hoechst 33342 (1 μg ml^{-1}) and ActinRed 555 ReadyProbes (2 drops ml^{-1}) (Life Technologies) in PBS for 30 min at room temperature as instructed by the supplier. Fluorescent images were then acquired using a spinning-disk confocal microscope from Nikon Instruments Inc., Eclipse Ti-E.

Magnetic actuation and steering

Both synthetic microswimmers and the immunobots were actuated and steered using a custom-made five-coiled electromagnetic setup mounted on an optical Zeiss inverted microscope (Zeiss Axio Observer A1) as previously described (*49*). Synthetic microswimmers were propelled and steered by applying a 5-mT rotating magnetic field inside both 1× PBS and whole blood (mouse CD1 whole blood, Innovative Research Inc., Pearly Court). The step-out frequencies were determined by gradually increasing the frequencies from 40 to 150 Hz.

An in-house tracking software developed in MATLAB (MathWorks, Natick, MA) was used for the mobility characterizations.

Statistical analysis

All experiments involving cells were carried out independently at least five times and three times for other experiments in addition to three technical replicates in each independent experiment. Unless otherwise mentioned, the values were reported as means ± SE of the mean. Student's *t* test and two-way analysis of variance (ANOVA) were performed using the software GraphPad Prism 6 (Graph Pad Inc.) to assess the statistical significance of differences in the results.

SUPPLEMENTARY MATERIALS

robotics.sciencemag.org/cgi/content/full/5/43/eaaz3867/DC1
Text
Fig. S1. Magnetic actuation setup and snapshots from the locomotion videos in whole blood.
Fig. S2. Twenty-four–hour viability assessment of J774A-1 cells interacting with microswimmers (tissue culture plate).
Fig. S3. SEM images of five-turn microswimmers made from PEGDA and their interactions with the macrophages.
Fig. S4. Time-lapse tracking of a microswimmer during phagocytosis.
Fig. S5. Flattening over the microswimmers by macrophages through membrane protrusions.
Fig. S6. Macrophage-microswimmer interactions.
Fig. S7. Macrophages accommodate themselves to internalize the microswimmers by growing their size.
Fig. S8. Size-phagocytosis relationship.
Fig. S9. Optical microscopy images of unstimulated splenocytes-microswimmer interactions over 96 hours.
Fig. S10. Optical microscopy images of LPS-stimulated splenocytes-microswimmer interactions after 24 and 48 hours.
Fig. S11. Optical microscopy images of LPS-stimulated splenocytes-microswimmer. interactions after 72 and 96 hours.
Fig. S12. Metabolic activity rate and proliferation of splenocytes interacting with microswimmers.
Fig. S13. Fluorescence intensity analysis of actin ring after the helical geometry of the microswimmers.
Fig. S14. Unstimulated splenocytes interacting with microswimmers.
Fig. S15. Rolling and rowing types of locomotion of the immunobots.
Fig. S16. Cell-powered autonomous motion of immunobots.
Table S1. Dimensions of the microswimmers.
Table S2. Forty-eight–hour interaction analysis of the non–serum-treated microswimmers with macrophages.
Table S3. Twenty-four–hour interaction analysis of the serum-treated microswimmers with macrophages.
Table S4. Dimensions of the grooves with respect to the length and turn number of the helical microswimmers.
Table S5. The overall number of microswimmers analyzed for interaction with splenocytes and percent internalization of the microswimmers after 96 hours of incubation.
Movie S1. Magnetic actuation of the synthetic microswimmers in 1× PBS and whole mouse blood.
Movie S2. Internalization of the adherent and free-floating microswimmers by macrophages.
Movie S3. Magnetic actuation of the immunobots.
Movie S4. Autonomous crawling of the immunobots and their trajectories.
Movie S5. Nonspecific adhesion of the synthetic microswimmers to the surrounding cells (semiadherent nonmagnetic macrophages), blocking their swimming locomotion.

REFERENCES AND NOTES

1. B. J. Nelson, I. K. Kaliakatsos, J. J. Abbott, Microrobots for minimally invasive medicine. *Annu. Rev. Biomed. Eng.* **12**, 55–85 (2010).
2. M. Sitti, H. Ceylan, W. Hu, J. Giltinan, M. Turan, S. Yim, E. Diller, Biomedical applications of untethered mobile milli/microrobots. *Proc. IEEE Inst. Electr. Electron. Eng.* **103**, 205–224 (2015).
3. F. Soto, R. Chrostowski, Frontiers of medical micro/nanorobotics: In vivo applications and commercialization perspectives toward clinical uses. *Front. Bioeng. Biotechnol.* **6**, 170 (2018).
4. H. Ceylan, J. Giltinan, K. Kozielski, M. Sitti, Mobile microrobots for bioengineering applications. *Lab Chip* **17**, 1705–1724 (2017).
5. P. Erkoc, I. C. Yasa, H. Ceylan, O. Yasa, Y. Alapan, M. Sitti, Mobile microrobots for active therapeutic delivery. *Adv. Therap.* **2**, 1800064 (2019).
6. Y. Alapan, O. Yasa, B. Yigit, I. C. Yasa, P. Erkoc, M. Sitti, Microrobotics and microorganisms: Biohybrid autonomous cellular robots. *Annu. Rev. Control Robot. Auton. Syst.* **2**, 205–230 (2019).
7. H. Ceylan, I. C. Yasa, K. Ugur, W. Hu, M. Sitti, Translational prospects of untethered medical microrobots. *Prog. Biomed. Eng.* **1**, 012002 (2019).
8. A. K. Simon, G. A. Hollander, A. McMichael, Evolution of the immune system in humans from infancy to old age. *Proc. Biol. Sci.* **282**, 20143085 (2015).
9. C. Varol, A. Mildner, S. Jung, Macrophages: Development and tissue specialization. *Annu. Rev. Immunol.* **33**, 643–675 (2015).
10. G. Sharma, D. T. Valenta, Y. Altman, S. Harvey, H. Xie, S. Mitragotri, J. W. Smith, Polymer particle shape independently influences binding and internalization by macrophages. *J. Control. Release* **147**, 408–412 (2010).
11. J. A. Champion, S. Mitragotri, Role of target geometry in phagocytosis. *Proc. Natl. Acad. Sci. U.S.A.* **103**, 4930–4934 (2006).
12. E. M. Purcell, Life at low Reynolds number. *Am. J. Phys.* **45**, 3–11 (1977).
13. X. Wang, C. Hu, L. Schurz, C. De Marco, X. Chen, S. Pané, B. J. Nelson, Surface-chemistry-mediated control of individual magnetic helical microswimmers in a swarm. *ACS Nano* **12**, 6210–6217 (2018).
14. H. Ceylan, I. C. Yasa, O. Yasa, A. F. Tabak, J. Giltinan, M. Sitti, 3D-printed biodegradable microswimmer for theranostic cargo delivery and release. *ACS Nano* **13**, 3353–3362 (2019).
15. H. Ceylan, I. C. Yasa, M. Sitti, 3D chemical patterning of micromaterials for encoded functionality. *Adv. Mater.* **29**, 1605072 (2017).
16. N. A. Alcantar, E. S. Aydil, J. N. Israelachvili, Polyethylene glycol-coated biocompatible surfaces. *J. Biomed. Mater. Res.* **51**, 343–351 (2000).
17. L. Zhang, J. J. Abbott, L. Dong, B. E. Kratochvil, D. Bell, B. J. Nelson, Artificial bacterial flagella: Fabrication and magnetic control. *Appl. Phys. Lett.* **94**, 064107 (2009).
18. A. Ghosh, P. Fischer, Controlled propulsion of artificial magnetic nanostructured propellers. *Nano Lett.* **9**, 2243–2245 (2009).
19. H. Kress, E. H. K. Stelzer, D. Holzer, F. Buss, G. Griffiths, A. Rohrbach, Filopodia act as phagocytic tentacles and pull with discrete steps and a load-dependent velocity. *Proc. Natl. Acad. Sci. U.S.A.* **104**, 11633–11638 (2007).
20. S. Schuerle, I. A. Vizcarra, J. Moeller, M. S. Sakar, B. Özkale, A. M. Lindo, F. Mushtaq, I. Schoen, S. Pané, V. Vogel, B. J. Nelson, Robotically controlled microprey to resolve initial attack modes preceding phagocytosis. *Sci. Robot.* **2**, eaah6094 (2017).
21. G. Gerisch, M. Ecke, B. Schroth-Diez, S. Gerwig, U. Engel, L. Maddera, M. Clarke, Self-organizing actin waves as planar phagocytic cup structures. *Cell Adh. Migr.* **3**, 373–382 (2009).
22. M. Goktas, G. Cinar, I. Orujalipoor, S. Ide, A. B. Tekinay, M. O. Guler, Self-assembled peptide amphiphile nanofibers and peg composite hydrogels as tunable ECM mimetic microenvironment. *Biomacromolecules* **16**, 1247–1258 (2015).
23. S. Tollis, A. E. Dart, G. Tzircotis, R. G. Endres, The zipper mechanism in phagocytosis: Energetic requirements and variability in phagocytic cup shape. *BMC Syst. Biol.* **4**, 149 (2010).
24. J. A. Champion, S. Mitragotri, Shape induced inhibition of phagocytosis of polymer particles. *Pharm. Res.* **26**, 244–249 (2009).
25. S. Mitragotri, J. Lahann, Physical approaches to biomaterial design. *Nat. Mater.* **8**, 15–23 (2009).
26. J. A. Champion, A. Walker, S. Mitragotri, Role of particle size in phagocytosis of polymeric microspheres. *Pharm. Res.* **25**, 1815–1821 (2008).
27. J. M. Anderson, A. Rodriguez, D. T. Chang, Foreign body reaction to biomaterials. *Semin. Immunol.* **20**, 86–100 (2008).
28. F. Meng, C. A. Lowell, Lipopolysaccharide (LPS)-induced macrophage activation and signal transduction in the absence of Src-family kinases Hck, Fgr, and Lyn. *J. Exp. Med.* **185**, 1661–1670 (1997).
29. P. C. Ke, S. Lin, W. J. Parak, T. P. Davis, F. Caruso, A decade of the protein corona. *ACS Nano* **11**, 11773–11776 (2017).
30. T. Ishida, N. Fujihara, T. Nishimura, H. Funabashi, R. Hirota, T. Ikeda, A. Kuroda, Live-cell imaging of macrophage phagocytosis of asbestos fibers under fluorescence microscopy. *Genes Environ.* **41**, 14 (2019).
31. P. Liao, L. Xing, S. Zhang, D. Sun, Magnetically driven undulatory microswimmers integrating multiple rigid segments. *Small* **15**, 1901197 (2019).
32. L. Ricotti, B. Trimmer, A. W. Feinberg, R. Raman, K. K. Parker, R. Bashir, M. Sitti, S. Martel, P. Dario, A. Menciassi, Biohybrid actuators for robotics: A review of devices actuated by living cells. *Sci. Robot.* **2**, eaaq0495 (2017).
33. X. Yan, Q. Zhou, M. Vincent, Y. Deng, J. Yu, J. Xu, T. Xu, T. Tang, L. Bian, Y.-X. J. Wang, K. Kostarelos, L. Zhang, Multifunctional biohybrid magnetite microrobots for imaging-guided therapy. *Sci. Robot.* **2**, eaaq1155 (2017).
34. O. Felfoul, M. Mohammadi, S. Taherkhani, D. de Lanauze, Y. Z. Xu, D. Loghin, S. Essa, S. Jancik, D. Houle, M. Lafleur, L. Gaboury, M. Tabrizian, N. Kaou, M. Atkin, T. Vuong,

G. Batist, N. Beauchemin, D. Radzioch, S. Martel, Magneto-aerotactic bacteria deliver drug-containing nanoliposomes to tumour hypoxic regions. *Nat. Nanotechnol.* **11**, 941–947 (2016).
35. H. Xu, M. Medina-Sánchez, V. Magdanz, L. Schwarz, F. Hebenstreit, O. G. Schmidt, Sperm-hybrid micromotor for targeted drug delivery. *ACS Nano* **12**, 327–337 (2018).
36. O. Yasa, P. Erkoc, Y. Alapan, M. Sitti, Microalga-powered microswimmers toward active cargo delivery. *Adv. Mater.* **30**, e1804130 (2018).
37. T. Yang, A. Tomaka, T. O. Tasci, K. B. Neeves, N. Wu, D. W. M. Marr, Microwheels on microroads: Enhanced translation on topographic surfaces. *Sci. Robot.* **4**, eaaw9525 (2019).
38. M. Medina-Sánchez, L. Schwarz, A. K. Meyer, F. Hebenstreit, O. G. Schmidt, Cellular cargo delivery: Toward assisted fertilization by sperm-carrying micromotors. *Nano Lett.* **16**, 555–561 (2016).
39. A. D. Bershadsky, M. M. Kozlov, Crawling cell locomotion revisited. *Proc. Natl. Acad. Sci. U.S.A.* **108**, 20275–20276 (2011).
40. S. Barzilai, S. K. Yadav, S. Morrell, F. Roncato, E. Klein, L. Stoler-Barak, O. Golani, S. W. Feigelson, A. Zemel, S. Nourshargh, R. Alon, Leukocytes breach endothelial barriers by insertion of nuclear lobes and disassembly of endothelial actin filaments. *Cell Rep.* **18**, 685–699 (2017).
41. Y.-S. Chu, W. A. Thomas, O. Eder, F. Pincet, E. Perez, J. P. Thiery, S. Dufour, Force measurements in E-cadherin–mediated cell doublets reveal rapid adhesion strengthened by actin cytoskeleton remodeling through Rac and Cdc42. *J. Cell Biol.* **167**, 1183–1194 (2004).
42. A. Barbot, thesis, Université Paris-Saclay (2016).
43. M. Muthana, S. D. Scott, N. Farrow, F. Morrow, C. Murdoch, S. Grubb, N. Brown, J. Dobson, C. E. Lewis, A novel magnetic approach to enhance the efficacy of cell-based gene therapies. *Gene Ther.* **15**, 902–910 (2008).
44. N. Landázuri, S. Tong, J. Suo, G. Joseph, D. Weiss, D. J. Sutcliffe, D. P. Giddens, G. Bao, W. Robert Taylor, Magnetic targeting of human mesenchymal stem cells with internalized superparamagnetic iron oxide nanoparticles. *Small* **9**, 4017–4026 (2013).
45. J. Riegler, A. Liew, S. O. Hynes, D. Ortega, T. O'Brien, R. M. Day, T. Richards, F. Sharif, Q. A. Pankhurst, M. F. Lythgoe, Superparamagnetic iron oxide nanoparticle targeting of MSCs in vascular injury. *Biomaterials* **34**, 1987–1994 (2013).
46. J. Han, J. Zhen, V. D. Nguyen, G. Go, Y. Csshoi, S. Y. Ko, J.-O. Park, S. Park, Hybrid-actuating macrophage-based microrobots for active cancer therapy. *Sci. Rep.* **6**, 28717 (2016).
47. M. Muthana, A. J. Kennerley, R. Hughes, E. Fagnano, J. Richardson, M. Paul, C. Murdoch, F. Wright, C. Payne, M. F. Lythgoe, N. Farrow, J. Dobson, J. Conner, J. M. Wild, C. Lewis, Directing cell therapy to anatomic target sites in vivo with magnetic resonance targeting. *Nat. Commun.* **6**, 8009 (2015).
48. N. Gunduz, H. Ceylan, M. O. Guler, A. B. Tekinay, Intracellular accumulation of gold nanoparticles leads to inhibition of macropinocytosis to reduce the endoplasmic reticulum stress. *Sci. Rep.* **7**, 40493 (2017).
49. I. C. Yasa, A. F. Tabak, O. Yasa, H. Ceylan, M. Sitti, 3D-printed microrobotic transporters with recapitulated stem cell niche for programmable and active cell delivery. *Adv. Funct. Mater.* **29**, 1808992 (2019).

Acknowledgments: We acknowledge K. Elflein and B. Pichler for supplying with fresh mouse spleens. We also thank D. Sheehan for help with the fluorescence-activated cell sorting analysis. **Funding:** This work was funded by the Max Planck Society. **Author contributions:** I.C.Y., H.C., and M.S. conceived and designed the study. I.C.Y. and H.C. designed the experiments and analyzed the data. I.C.Y. performed the fabrication of the microswimmers, the internalization experiments, and imaging. H.C. performed the enzyme-linked immunosorbent assay studies and analyzed cell-macrophage interactions. U.B. performed the swimming analyses. A.-M.W. contributed to the experiments with splenocytes. I.C.Y., U.B., H.C., and M.S. contributed to the writing of the manuscript. All authors have given their consent to the final version of the manuscript. **Competing interests:** The authors declare that they have no competing interests. **Data and materials availability:** All data needed to evaluate the conclusions of the paper are available in the paper or the Supplementary Materials. Contact M.S. for materials.

Submitted 4 September 2019
Resubmitted 19 January 2020
Accepted 13 May 2020
Published 17 June 2020
10.1126/scirobotics.aaz3867

Citation: I. C. Yasa, H. Ceylan, U. Bozuyuk, A.-M. Wild, M. Sitti, Elucidating the interaction dynamics between microswimmer body and immune system for medical microrobots. *Sci. Robot.* **5**, eaaz3867 (2020).

Science Robotics

Elucidating the interaction dynamics between microswimmer body and immune system for medical microrobots

Immihan Ceren Yasa, Hakan Ceylan, Ugur Bozuyuk, Anna-Maria Wild, and Metin Sitti

Sci. Robot. **5** (43), eaaz3867. DOI: 10.1126/scirobotics.aaz3867

Science Robotics (ISSN 2470-9476) is published by the American Association for the Advancement of Science. 1200 New York Avenue NW, Washington, DC 20005. The title *Science Robotics* is a registered trademark of AAAS.